The ATAL within the 2017 Asian Monsoon Anticyclone: Microphysical aerosol properties derived from aircraft-borne in situ measurements

Christoph Mahnke[1,*], Ralf Weigel[2], Francesco Cairo[3], Jean-Paul Vernier[4,5], Armin Afchine[6], Martina Krämer[6], Valentin Mitev[7], Renaud Matthey[8], Silvia Viciani[9], Francesco D'Amato[9], Felix Ploeger[6], Terry Deshler[10], and Stephan Borrmann[1,2]

[1]Particle Chemistry Department, Max Planck Institute for Chemistry, Mainz, Germany
[2]Institute for Atmospheric Physics, Johannes Gutenberg University, Mainz, Germany
[3]Institute of Atmospheric Sciences and Climate, ISAC-CNR, Rome, Italy
[4]National Institute of Aerospace, Hampton, Virginia, USA
[5]NASA Langley Research Center, Hampton, Virginia, USA
[6]Institute of Energy and Climate Research - IEK7, Forschungszentrum Jülich, Jülich, Germany
[7]Centre Suisse d'Electronique et de Microtechnique, CSEM SA, Neuchâtel, Switzerland
[8]Institut de Physique, Université de Neuchâtel, Neuchâtel, Switzerland
[9]National Institute of Optics, CNR-INO, Sesto Fiorentino, Italy
[10]Department of Atmospheric Science, University of Wyoming, Laramie, Wyoming, USA
[*]now at: Institute of Energy and Climate Research - IEK8, Forschungszentrum Jülich, Jülich, Germany

Correspondence: Christoph Mahnke (c.mahnke@fz-juelich.de)

Abstract. The Asian summer monsoon is an effective pathway for aerosol particles and precursor substances from the planetary boundary layer over Central, South, and East Asia into the upper troposphere and lower stratosphere. An enhancement of aerosol particles within the Asian monsoon anticyclone (AMA) has been observed by satellites, called the Asian Tropopause Aerosol Layer (ATAL). In this paper we discuss airborne in situ and remote sensing observations of aerosol microphysical properties conducted during the 2017 StratoClim field campaign within the region of the Asian monsoon anticyclone. The aerosol particle measurements aboard the high-altitude research aircraft M55 Geophysica (reached a maximum altitude of about 20.5 km) were conducted by a modified Ultra High Sensitivity Aerosol Spectrometer Airborne (UHSAS-A; particle diameter detection range from 65 nm to 1 µm), the COndensation PArticle counting System (COPAS, for detecting total aerosol densities of submicrometer sized particles), and the Cloud and Aerosol Spectrometer with Detection of POLarization (NIXE-CAS-DPOL). In the COPAS and UHSAS-A vertical particle mixing ratio profiles, the ATAL is evident as a distinct layer between 15 km ($\approx$ 370 K) and 18.5 km altitude ($\approx$ 420 K potential temperature). Within the ATAL, the maximum detected particle mixing ratios (from the median profiles) were 700 $\mathrm{mg^{-1}}$ for diameters between 65 nm to 1 µm (UHSAS-A) and higher than 2500 $\mathrm{mg^{-1}}$ for diameters larger than 10 nm (COPAS). These values are up to two times higher than previously found at similar altitudes in other tropical locations. The difference between the particle mixing ratio profiles measured by the UHSAS-A and the COPAS indicate that the region below the ATAL at potential temperatures from 350 to 370 K is influenced by the fresh nucleation of aerosol particles (diameter < 65 nm). We provide detailed analyses of the vertical distribution of the aerosol particle size distributions and the particle mixing ratios and compare these with previous tropical

and extratropical measurements. The aerosol scattering ratio was calculated based on the in situ measured aerosol particle
size distributions. The resulting dataset was compared with the vertical profiles of the aerosol scattering ratios detected by the

20 Multiwavelength Aerosol Scatterometer (MAS) and an airborne Miniature Aerosol Lidar (MAL) aboard the M55 Geophysica
and by the satellite-borne Cloud-Aerosol Lidar with Orthogonal Polarization (CALIOP). The data of all four methods largely
agree with each other, showing enhanced values of aerosol scattering ratio in the altitude range of the Asian Tropopause Aerosol
Layer with a maximum at 17.5 km altitude. By means of the AMA-centered equivalent latitude calculated from meteorological
reanalysis data it is shown that such enhanced values of the aerosol scattering ratio larger 1.08 could only be observed within

25 the confinement of the Asian monsoon anticyclone.

1   Introduction

During the Asian Summer Monsoon (ASM) the Upper Troposphere / Lower Stratosphere (UT/LS) over the Indian subcontinent
is strongly influenced by the Asian Monsoon Anticyclone (AMA). Inside the AMA, the ATAL (Asian Tropopause Aerosol
Layer) was discovered from faint signals of satellite borne lidar measurements (Vernier et al. (2009); Vernier et al. (2011);

30 Vernier et al. (2018)). Its vertical extent typically ranges from 14 to 18 km altitude corresponding to 360 K and 420 K potential
temperature levels, respectively. The AMA develops periodically during the summer of the northern hemisphere (Park et al.
(2007)), covering a vertical extent from about 12 to 18 km altitude and has its maximum strength at 17 to 18 km, around
the local tropopause (Ploeger et al. (2015); Brunamonti et al. (2018)). With the large variability in its horizontal extent, the
AMA covers longitudes from Northeastern Africa to East Asia (Pan et al. (2016); Vogel et al. (2019)). The dynamic processes

35 associated with the AMA provide the setting for an effective vertical transport of trace substances from the lower troposphere
accompanied with a certain level of accumulation within the anticyclone. These processes affect the composition of trace gases,
particle precursor gases and aerosol particles in all levels of the UT/LS at different intensities (Randel and Park (2006); Park
et al. (2009) Randel and Jensen (2013); Vogel et al. (2015); Pan et al. (2016); Bucci et al. (2020)).

The AMA is a prominent feature with a closed, quasi-rotational circulation in the UT/LS, which is confined by a westerly

40 jet stream in the mid-latitudes and an easterly jet stream in the tropics (Dunkerton (1995); Pan et al. (2016); Brunamonti
et al. (2018)). Associated with the AMA are large convective systems during monsoon times which provide efficient vertical
transport routes for trace substances, aerosol precursors, and aerosol particles from the boundary layer to the altitude levels
of the AMA, the Tropical Tropopause Layer (TTL), and the lower stratosphere (Fueglistaler et al. (2009)). The lifted material
includes anthropogenic releases from ground level pollution such as ammonia which forms ammonium nitrate particles in the

45 troposphere (Höpfner et al. (2019)), which can impact ice cloud formation in the Asian monsoon upper troposphere (Wagner
et al. (2020)). The TTL, which in this area extends over an altitude range of about 14 to 18 km, acts as a "gateway to the
stratosphere" (Fueglistaler et al. (2009)), because from here, air can be transported into the lower stratosphere via diabatic
ascent (Garny and Randel (2016)). With the transport of climate-relevant natural and anthropogenic trace gases, water vapor,
and aerosol particles into the stratosphere, also precursor gases enter the UT/LS, which can lead or contribute to the formation

50 of new particles from the gas phase (New Particle Formation, NPF) (Brock et al. (1995); Weigel et al. (2011); Williamson

et al. (2019)). Asia is currently one of the regions with the highest production of atmospheric sulphur worldwide. Therefore, the vertical transport of these sulphur-containing aerosol particles and particle precursor gases, through the high-reaching convection of the ASM, can influence the chemical balance of the stratosphere and the climate (Vernier et al. (2011); Kremser et al. (2016)). This was initially suggested as cause for the ATAL (Vernier et al. (2011); Neely et al. (2014); Yu et al. (2015)),
55 however, Höpfner et al. (2019) demonstrated that ammonium nitrate formed from gaseous ammonia in the higher troposphere is an important if not the dominant component of the ATAL aerosol. Furthermore, model analysis (with the GEOS-Chem transport model) by Fairlie et al. (2020) indicate the dominance of regional anthropogenic emissions from China and the Indian subcontinent to aerosol concentrations in the ATAL.

For a more detailed analysis of these processes, airborne measurements of the microphysical properties of aerosol particles
60 are discussed in this study. These measurements were conducted during the 2017 StratoClim field campaign at the time of the ASM. We took a closer look at the vertical distribution of the submicrometric aerosol particle mixing ratio and the aerosol particle size distributions within the AMA region. Balloon-borne in situ aerosol backscatter measurements from Vernier et al. (2015), Yu et al. (2017), Brunamonti et al. (2018), and Vernier et al. (2018) confirmed the enhanced aerosol signal observed by Vernier et al. (2011) since 2006. In order to relate their observations with our in situ observations obtained during StratoClim
65 2017, we calculated the theoretically expected aerosol particle scattering ratio based on our in situ measured aerosol particle size distributions. With a focus on the ATAL region, we compare these results with observations from the satellite-borne Cloud-Aerosol Lidar with Orthogonal Polarization (CALIOP) (Winker et al. (2010); Vernier et al. (2011)), the airborne backscatter probe MAS (Sec. 3.4) and the airborne lidar MAL (Sec. 3.5) during StratoClim 2017.

2 The StratoClim field campaigns in the Mediterranean (2016) and the Asian summer monsoon region (2017)

70 The 2017 StratoClim (Stratospheric and upper tropospheric processes for better climate prediction) field campaign took place in July and August in Kathmandu (Nepal). The goal of StratoClim is to gain a better understanding of the key processes in the upper troposphere and stratosphere of the ASM region in order to better assess the effects on climate change and stratospheric trace gases including ozone. The StratoClim project includes a measurement campaign with airborne and balloon-borne measurements (based on tropical ground stations at different locations on the Indian subcontinent), satellite-based observations
75 and process-related, regional and global model studies. The choice of Kathmandu as a base for the M55 Geophysica research aircraft allowed measurements to be carried over Nepal, India, Bangladesh and the Bay of Bengal within the AMA. The M55 Geophysica was equipped with extensive equipment to measure aerosol and cloud microphysics, aerosol chemistry, trace gases, radiation, and other basic meteorological parameters. The 2017 StratoClim measurement campaign included eight mission flights based in Kathmandu (Nepal) Tribhuvan International Airport (TIA) with a total flight time of about 31 hours
80 (flight paths see Fig. 1). Out of the eight measurement flights, three (KTM2, KTM4, and KTM5) took place exclusively in the Nepalese airspace. These flights were carried out along an axis parallel to the Himalayan mountains over almost the entire east-west extension of Nepal. Three further measurement flights (KTM3, KTM7, and KTM8) were headed to India. This allowed studying the horizontal structure of the AMA over large parts of its north-south extension. Bucci et al. (2020) showed

that the first half of the StratoClim 2017 campaign period was less affected by regional convective activity compared to the
85   second half, allowing to observe the ATAL under "dry" conditions (flights KTM1 to KTM4) and under convective influence
(flights KTM5 to KTM8).

    Also included in our analyses are measurements from the first phase of the StratoClim campaign which took place in 2016
and was based from Kalamata, Greece (37° N, 22° E). During this campaign phase three flights reaching up to 20 km altitude
were conducted in the Mediterranean region (30 August, 1 September, and 6 September) using the M55 Geophysica. The
90   results from these extratropical aerosol measurements are juxtaposed to the tropical data from the ASM during StratoClim
2017.

3   Instrumentation on the M55 Geophysica high-altitude research aircraft

The main instrument used for the measurements discussed in this study is the Ultra High Sensitivity Aerosol Spectrometer
Airborne (UHSAS-A). Besides the UHSAS-A, in situ and remote sensing instruments aboard the M55 Geophysica were
95   included for the analyses discussed in this study: The in situ particle instruments COPAS and NIXE-CAS, the backscatter
probe MAS, the air-borne lidar MAL, and the carbon monoxide instrument COLD2. The basic meteorological parameters and
the avionic data from the M55 Geophysica is provided by the Unit for Connection with Scientific Equipment (UCSE; Sokolov
and Lepuchov (1998)).

3.1   The UHSAS-A

100   The UHSAS-A is the wing-sonde version of the UHSAS (Cai et al. (2008)), a laser-based aerosol spectrometer designed and
manufactured by Droplet Measurement Technologies (DMT, Boulder, Colorado, USA). It is designed for airborne operation
at altitudes of up to 12 km and is able to measure aerosol particle number size distributions in the diameter range from 65 to
1000 nm at 1 Hz sampling frequency.

    For operations at altitudes up to 20 km under tropical, stratospheric ambient conditions aboard the research aircraft M55
105   Geophysica two major modifications of the standard version of the UHSAS-A had been necessary. Integrating a pressure
sensor measuring the air pressure in the optical measurement cell of the UHSAS-A and a new pump system enabling constant
system flows even under low stratospheric air pressures. The stability of the sample, sheath, and purge flow was first tested
within a low pressure chamber, before the StratoClim 2017 field campaign. This low pressure chamber tests were conducted
under air pressure values down to 45 hPa within the UHSAS-A measurement cell. Also, during the operation aboard the
110   M55 Geophysica the sample, sheath, and purge flow were stable and constant throughout all StratoClim 2017 mission flights.
Additionally, the new dual headed membrane pump system, installed in the UHSAS-A, minimizes the pulsation of the flow
within the UHSAS-A measurement cell compared to a single headed membrane pump. The sample flow measurement was
characterized pressure dependent. For this purpose the UHSAS-A was located in the low pressure chamber and connected
through a chamber outlet via a high precision needle valve to a reference flow meter (Gilibrator Version 2 by SENSIDYNE).

Prior to the 2017 StratoClim field campaign the UHSAS-A has been calibrated with Polystyrol Latex spheres (PSL, Thermo Fisher Scientific) with diameters of 102, 147, 296 and 799 nm. During the calibration process the PSL particles were classified with a differential mobility analyzer (DMA, TSI 3080 with TSI 3081). During the field campaign in Nepal, before every mission flight the calibration of the UHSAS-A was validated with the same PSL calibration standards. The uncertainty of the measured number concentration was determined to be lower than 10 % based on laboratory characterization. This is valid as long as the statistical counting error is also lower than 10 %. For the 1 Hz resolved measurements, this is the case for ambient particle number concentrations larger than $100 \, \mathrm{cm}^{-3}$. At ambient particle number concentrations as low as $1 \, \mathrm{cm}^{-3}$ the data should be averaged over time intervals of about 100 seconds to gain sufficient counting statistics. Due to missing in-line temperature measurements and the wide ambient temperature range during StratoClim, the uncertainty of the UHSAS-A measurements is estimated to be up to 25 %.

3.2 COPAS

The COndensation PArticle counting System (COPAS) consists of two separate units, each containing two separate condensation particle counters. Three of the condensation particle counters detect all aerosol particles with diameters larger than 6 nm, 10 nm, and 15 nm, respectively. The upper limit of the particle diameter detection range is determined with respect to the characteristics of the aerosol inlet system to about one micrometer in diameter. This describes the limit, up to which particles are aspirated with almost 100 % efficiency and transported through the aerosol lines to the detector. The fourth condensation particle counter detects the aerosol particles with diameters larger than 10 nm, which have previously passed through a heated tube section (at 270 °C) of about one meter length. Therefore, this channel detects residual particle cores which are non-volatile at this temperature. The COPAS has been characterized in Weigel et al. (2009) and the application of the heated channel has been adopted for several studies (Curtius et al. (2005); Borrmann et al. (2010); Weigel et al. (2011); Weigel et al. (2014); Weigel et al. (2020a)).

3.3 NIXE-CAS

The Cloud and Aerosol Spectrometer with Detection of POLarization (NIXE-CAS-DPOL, here referred to as NIXE-CAS) is part of the New Ice eXpEriment Cloud and Aerosol Particle Spectrometer (NIXE-CAPS) underwing probe. Together with the Cloud Imaging Probe greyscale (NIXE–CIPg), the NIXE-CAPS can measure the particle size distribution for larger aerosol particles as well as cloud particles within a diameter range from 0.61 to 937 μm (Costa et al. (2017)). The overall measurement uncertainties of the particle number concentrations and the particle sizing are estimated to be approximately 20 % by Costa et al. (2017), more detailed descriptions of the instruments performance and measuring principles are given by Baumgardner et al. (2017). For this study, the lowest size bins of NIXE-CAS (0.61 to 3 μm) have been used to provide additional information extending beyond the upper detection limit of the UHSAS-A, as such large aerosol particles potentially influence the derived scattering ratios.

3.4 MAS

The Multiwavelength Aerosol Scatterometer (MAS) is an elastic backscatter near range lidar that operates at wavelengths of 532 or 1064 nm. It measures the backscatter and the depolarization from cloud and aerosol particles like a remote sensing lidar, but in situ in a range of 3 to 30 m close to the aircraft. It is capable of measuring at a time resolution of 5 to 10 seconds,

150   what translates to a horizontal resolution of 1 to 2 km, considering the M55 Geophysicas cruising speed of about 170 m s^{-1}. Its technical details and analysis of its measurement performance aboard the M55 Geophysica are discussed in detail by Cairo (2004), Cairo et al. (2011), and Molleker et al. (2014).

3.5 MAL

The Miniature Aerosol Lidar (MAL) aboard the M55 Geophysica is a combination of two identical stand-alone airborne lidar

155   systems, one facing upwards and the other facing downwards. The two microjoule backscatter-depolarisation lidar systems operate at a wavelength of 532 nm and are capable of measuring range-resolved backscatter and depolarization profiles along the aircraft flight track, 2 km above and underneath the aircraft. Previous applications of the MAL lidar are discussed in publications by Cairo (2004), Mitev et al. (2014), and Molleker et al. (2014). During the RECONCILE campaign a comparison study between the MAL lidar aboard the M55 Geophysica and the satellite-borne CALIOP lidar was conducted by Mitev et al.

160   (2012).

3.6 COLD2

During the 2017 StratoClim field campaign, the Carbon Monoxide (CO) mixing ratio was measured in situ by COLD2 (Carbon Oxide Laser Detector 2), the newly improved version of the Cryogenically Operated Laser Diode spectrometer (COLD) aboard the M55 Geophysica. The previous version COLD, based on lead salts laser, operating around liquid nitrogen temperature, was

165   successfully operated during several tropospheric and stratospheric measurement campaigns since 2005 and its functionality is described in detail by Viciani et al. (2008). The present instrument is based on a room temperature quantum cascade laser and an updated electronics, with a substantial reduction of weight and dimensions, and no more need of cryogenic fluids. The detection principle of the COLD instruments is based on the Tunable Diode Laser Spectroscopy. During the 2017 StratoClim operation, the COLD2 instrument attained an in-flight sensitivity of 1 to 2 ppb with a time resolution of 1 Hz and an accuracy

170   of 3 % (Viciani et al. (2018)). In this study the CO measurements are adopted as tracer for air masses affected by pollution or biomass burning.

4   The vertical distribution of the aerosol particle mixing ratio within the AMA

The identification of transport and nucleation processes (i.e. New Particle Formation, NPF) of aerosol particles in the UT/LS and their influence on the radiation balance and chemistry of the atmosphere requires the knowledge of the vertical distribution

175   of the aerosol particle properties, such as particle size and number concentration. Figure 2 (a) shows the vertical distribution of

the particle mixing ratio (given in number of particles per mg of ambient air) as measured by the UHSAS-A during all research flights of the StratoClim 2017 measurement campaign. The potential temperature (Θ) is used as the vertical coordinate. To ease the recognition of the variability between the individual flights, the measured particle mixing ratios (1 Hz temporal resolution) are marked by data points of different color. In black, the median of the particle mixing ratio of all eight measurement flights,

180 calculated over 5 K potential temperature intervals, is plotted together with the 25% and 75% percentiles as horizontal bars to each median value. The number of 1 Hz data points included in each 5 K potential temperature interval is indicated in Fig. 2 (b).

Following the median of the particle mixing ratio from very high values (about $1500 \ \text{mg}^{-1}$) close to the ground level (Θ = 310 K), the particle mixing ratio decreases by an order of magnitude to about $150 \ \text{mg}^{-1}$ up to a potential temperature of 330

185 K. As evident from the 1 Hz resolved data, particle mixing ratios of up to $10000 \ \text{mg}^{-1}$ are measured between 310 and 330 K. Up to the Θ level of 345 K, the median particle mixing ratio remains at about $150 \ \text{mg}^{-1}$. The variability of the measurement results increases with altitude, which can be seen from the changes in the deviation of the 25% and 75% percentiles with respect to the median.

From 345 K to 350 K potential temperature, the median value inclines to a particle mixing ratio of $300 \ \text{mg}^{-1}$ until it

190 reaches a maximum of $700 \ \text{mg}^{-1}$ at about 365 to 370 K potential temperature. Between 350 and 370 K the 1 Hz data shows a high variability of the particle mixing ratio, both between the different flights, but also when the flights are considered individually. Particle mixing ratios between $6 \ \text{mg}^{-1}$ and over $10000 \ \text{mg}^{-1}$ were measured here. This high variability is also visible in the percentiles. Apart from the variability of the sampled airmasses inherent from the dynamics of the AMA, causes for such variability may also be the occurrence of New Particle Formation events (NPF) and scavenging by the large persistent

195 convective cloud systems. In these cloud systems many aerosol particles are activated to form condensation nuclei of cloud droplets or get washed out by scavenging, resulting in the observed very low aerosol particle mixing ratios (Croft et al. (2010); Yang et al. (2015)). On the other hand, these strong convective systems can lead to vertical transport of polluted air from the boundary layer, with high particle mixing ratios, up to high altitudes. A possible cause for the high particle mixing ratios in this altitude range, and sometimes up to 380 K potential temperature (flight KTM8), can also be the nucleation of aerosol particles

200 from precursor gases (NPF). These precursor gases of natural and anthropogenic origin are also subject to vertical transport by deep convective cloud systems reaching the TTL and cause NPF in case of favorable thermodynamic conditions (Borrmann et al. (2010); Höpfner et al. (2019); Weigel et al. (2020a); Weigel et al. (2020b)). The lapse rate tropopause (LRT in Fig. 2 (a)) during the 2017 campaign period was located between 369 and 396 K at a mean Θ level of about 380 K based on European Centre of Medium-Range Weather Forecasts (ECMWF) ERA-Interim reanalysis data. Above the tropopause region, starting at

205 about 380 K potential temperature, the variability of the particle mixing ratio begins to abate.

Up to a potential temperature of 420 K, the median of the particle mixing ratio decreases to about $80 \ \text{mg}^{-1}$, except for a local maximum at a potential temperature of 390 K. From there, up to a potential temperature of 445 K, the particle mixing ratio decreases further to a median of about $40 \ \text{mg}^{-1}$. Up to about 475 to 480 K, the highest Θ levels reached during the StratoClim 2017 measurement campaign, the median of the particle mixing ratio remains between 40 and $50 \ \text{mg}^{-1}$. Especially

210 for potential temperatures larger than 420 K and low particle mixing ratios in the range of 10 to $100 \ \text{mg}^{-1}$ it is noticeable,

that the 1 Hz data points form a vertical and slightly inclined discrete stripe pattern towards larger particle mixing ratios. This is due to the weak counting statistics of the single 1 Hz data points at these concentrations in combination with the constantly regulated sample flow (of $50 \text{ cm}^3 \text{ min}^{-1}$). However, due to the high number of 1 Hz data points (about 400 to 4000) available for each 5 K interval, even in this Θ range we are able to calculate robust median values with the given Θ resolution.

215   For relating these UHSAS-A results to the particle mixing ratios observed in other tropical and subtropical UT/LS regions, two data sets from the tropics as well as two sets from the extratropics were selected. These measurements were conducted with the COPAS instrument (described in Sec. 3.2) during the 2016 StratoClim field campaign in Greece (extratropics) and StratoClim 2017 in Nepal (tropics), as well as air-borne measurements within the tropics and the extratropics, published in Borrmann et al. (2010) and read out of Fig.1 from the publication by Brock et al. (1995). Figure 3 (a) shows the median
220   profiles of the COPAS measurement series from the 2016 and 2017 StratoClim campaigns together with the median profile from the 2017 StratoClim UHSAS-A data set. In addition to the tropical and extratropical profiles from Brock et al. (1995), Fig. 3 (b) compares the UHSAS-A and COPAS measured profiles from StratoClim 2017 (Nepal) with three further profiles measured by the COPAS instrument within the tropics during the field campaigns SCOUT-AMMA 2006 (West Africa, red line), SCOUT-O3 2005 (Northern Australia, red dotted line), and TROCCINOX 2005 (Brazil, green dotted line), discussed by
225   Borrmann et al. (2010) and Fierli et al. (2011).

In the region of the upper troposphere with potential temperatures between about 350 and 370 K, the median of the particle mixing ratio measured by COPAS during StratoClim 2017 (green line) reaches its maximum of 6000 mg^{-1}. A maximum (particle mixing ratio up to about 6500 mg^{-1}) that was also observed by Brock et al. (1995) in the tropical Central Pacific (orange line). The median of the UHSAS-A measurement remains almost constant in this Θ range with significantly lower
230   values of the particle mixing ratio of about 250 mg^{-1}. However, the variability of the particle mixing ratio measured by the UHSAS-A is, as discussed above, very high in this Θ range. The COPAS measurements shown here cover the particle diameter range from 10 to about 1000 nm, while the UHSAS-A detects aerosol particles in the diameter range from 65 to 1000 nm. The difference in the particle mixing ratios between the median values of the COPAS and the UHSAS-A measurements of about 5750 mg^{-1} shows, that very small aerosol particles between 10 and 65 nm in diameter dominate the aerosol total number
235   densities. This indicates that especially the Θ range between 350 and 370 K is influenced by the fresh nucleation of aerosol particles (NPF), what has also been shown by Weigel et al. (2020a) and Weigel et al. (2020b).

During the ASM, between about 370 and 415 K potential temperature, the median profile of the UHSAS-A data shows particle mixing ratios that are up to two times higher than the median profile observed by Brock et al. (1995) in extratropical regions (see Fig. 3 (b)). This is particularly noticeable since the particle mixing ratios of Brock et al. (1995) cover particle
240   diameters from 8 to 3000 nm and the UHSAS-A only detects aerosol particles in the diameter range from 65 to 1000 nm. The median profile of the COPAS measurement during the StratoClim 2016 measurement campaign in Greece (blue line) also shows lower particle mixing ratios than the comparative measurement within the AMA region (green). Compared with the extratropical COPAS measurements from StratoClim 2016, the UHSAS-A vertical profile shows mostly lower particle mixing ratios. However, in contrast to the UHSAS-A, the measurements with the COPAS also include very small aerosol
245   particles starting from 10 nm in diameter (starting from 6 nm during TROCCINOX 2005). Thus, inside the AMA, higher

particle mixing ratios were observed for the size diameter range from 65 to 1000 nm at altitudes between roughly 370 and 415 K than during similar measurements in the extratropics which include even much smaller particles (starting from 8 nm (Brock et al. (1995))). This enhanced aerosol mixing ratio can be associated with the ATAL discovered by Vernier et al. (2009), who observed the ATAL in about the same altitude range with potential temperatures between 370 and 420 K on the basis

250 of satellite-borne lidar measurements. Figure 3 (b) shows that such a maximum between roughly 340 and 390 K was also observed in the fine particle mixing ratios obtained from COPAS in other tropical locations (Northern Australia, West Africa, and Brazil; Borrmann et al. (2010)) albeit with significantly lower absolute values than for the AMA region. The increase in particle mixing ratio for altitudes above the 420 K level over West Africa was explained by Borrmann et al. (2010) as influence of the 2006 Soufrière Hills eruption in the Caribbean (also discussed by Prata et al. (2007) and Vernier et al. (2009)). In panel

255 (a) of Fig. 3 a subtle decrease of the UHSAS and COPAS mixing ratios from about 170 to 80 mg^{-1} and from 470 to 170 mg^{-1} respectively can be seen between the 410 and 420 K potential temperature levels. The altitude levels of this decrease roughly coincide with the top of the 2017 AMA circulation system (von Hobe et al. (2020)). Aloft the particle mixing ratios are mainly controlled by the large scale isentropic transport in the lowermost stratosphere and are less influenced by the AMA.

5   The vertical profile of the aerosol particle size distribution within the Asian monsoon anticyclone

260 Characterizing the ATAL, described by Vernier et al. (2011), requires knowledge about the aerosol particle size distribution's vertical profile. Within UT/LS altitudes, it is also important for the analysis of NPF events, cloud formation, and transport processes as well as for the calculation of the radiative balance and parameters like aerosol volume density (Höpfner et al. (2019)) and aerosol surface area, available for heterogeneous chemical conversion processes.

The results shown here are the first measurements made with a UHSAS-A in the tropical lower stratosphere. The performance

265 of the modified UHSAS-A (see Sec. 3.1) as evident from its technical parameters has been thoroughly tested in laboratory. To further demonstrate the profoundness of the in situ measurements at altitude, a comparison was made with other optical particle counter measurements of the aerosol particle size distributions from the stratosphere.

For this purpose we chose two measurements conducted with a balloon-borne set-up which continues the series of in situ data described in Deshler et al. (2003), Ward et al. (2014), and Deshler et al. (2019). The comparison measurements were from

270 Hyderabad (India) in August 2015, also during the ASM period, and from Laramie (United States of America) in August 2013. The optical particle counters (LPC; Laser Particle Counter) used for the measurements from Hyderabad and Laramie were operated with a particle diameter detection range from 0.18 to 32 μm and 0.18 to 9 μm, respectively. In both cases total particle concentration measurements were made with a condensation nuclei counter (CNC) with a nominal detection diameter of 20 nm (Campbell and Deshler (2014)), flown in parallel with the LPCs. The resulting particle size distributions are compared in

275 Fig. 4 with the data of the UHSAS-A obtained at the highest flight level (56 hPa pressure level) of the StratoClim mission flight KTM4. In each case the data set (500 m vertical averaging interval) was chosen for which the altitude range corresponded mostly to the flight level of the M55 Geophysica during the UHSAS-A measurements.

Considering the higher size resolution of the UHSAS-A and the difference in the detection range compared to the balloon-borne instrumentation, a sufficient agreement of the measurement results can be seen. In particular, the comparative measurement from Hyderabad (India), which also took place during the ASM, shows very good agreement between the CNC and UHSAS-A for particles < 0.18 μm and between the LPC and UHSAS-A for particles between 0.3 and 0.6 μm. Taking the temporal and spatial distance between these measurements into account, this comparison further indicates the quality of the measurements conducted with the modified UHSAS-A.

Figure 5 shows the vertical profile of the aerosol size distribution measured by the UHSAS-A averaged over the full StratoClim 2017 campaign period. The profile was averaged with a vertical resolution of 1 K potential temperature. The particle number concentrations for the size distributions' diameter bins are color-coded and normalized according to the bin-widths in terms of dN/dlogDp. To be able to compare the measured number concentrations of the size distributions over the full altitude range, the ambient number concentrations have been converted to Standard Temperature and Pressure (STP; $T_0 = 273.15$ K; $p_0 = 1013$ hPa) using the ambient temperature and pressure measurements reported by the UCSE.

Starting at a Θ level of 320 K, the profile of the aerosol particle size distribution has a pronounced maximum at the lower end of the UHSAS-A detection size range (diameter between 65 and 80 nm), together with enhanced number concentrations also for the large aerosol particles, with diameters up to 1000 nm. Until about 326 K potential temperature, the size distributions maximum is located between particle diameters of 70 and 80 nm and the overall number concentration decreases. This is especially the case for particles with a diameter larger than 600 nm. Up to potential temperatures of about 350 K the overall shape of the size distribution remains mostly constant. In the Θ range between 350 and 370 K the aerosol size distribution is very variable. It shows high number concentrations also for large particles up to 1000 nm in diameter, at the upper detection size-range of the UHSAS-A, and a very pronounced Aitken-mode. Above 370 K potential temperature the main mode of the size distribution broadens and shifts its maximum to diameters of about 100 nm. At about 395 K potential temperature the concentrations, especially for larger particles, begin to decrease. Above 420 K, until the maximum ceiling during StratoClim 2017, the shape of the aerosol size distribution shows only low variability. Altogether, for the 2017 AMA the measured vertical profiles of the aerosol size distributions show the presence of an ATAL feature between approximately 370 and 420 K with the peak of the size distributions in the 80 to 200 nm diameter range. We show here the first size-resolved aerosol vertical profiles measured aircraft-borne over the Indian subcontinent up to over 20 km altitude.

6 Backscatter properties of the ATAL - results from in situ and remote sensing instruments

The ATAL was first discovered and assessed by Vernier et al. (2009) and Vernier et al. (2011) in terms of an enhancement of the reanalyzed and cloud-filtered scattering ratio (SR) signal from the CALIOP lidar aboard the Cloud-Aerosol Lidar and Infrared Pathfinder Satellite Observations (CALIPSO) satellite. Vernier et al. (2015), Yu et al. (2017), and Vernier et al. (2018) could already confirm this enhancement using balloon-borne in situ backscatter and aerosol particle number concentration measurements. To go one step further, we calculated the SR based on the in situ measured aerosol particle size distributions

310   from the StratoClim 2017 campaign and compare it with the cloud-filtered CALIOP, MAS (Sec. 3.4), and MAL (Sec. 3.5) measurements for a mostly overlapping time period in 2017.

6.1   Method

For this analysis, all 8 measurement flights from the StratoClim 2017 campaign are divided into segments of 100 seconds. Segments in which cloud particles have been detected by the NIXE-CAS are removed from the data set to be consistent with

315   the cloud filtered CALIOP, MAS, and MAL data sets. To ensure a high vertical resolution, flight segments with ascending or descending rates which result in a potential temperature range higher than 5 K within the 100 seconds flight segment are removed as well.

For each remaining flight segment a UHSAS-A measured aerosol particle size distribution was averaged. The size range of this size distributions is extended from 65 - 1000 nm to 10 - 3000 nm using measurements conducted by the COPAS (Sec. 3.2)

320   and NIXE-CAS (Sec. 3.3) instruments.

One size-bin from 10 to 65 nm in diameter was calculated by subtraction of the UHSAS-A measured total number concentration (particle diameter range: 65 - 1000 nm) from the particle number concentration measured by the COPAS N_{10} channel (particle diameter range: 10 to about 1000 nm) described in Sec. 3.2. The measurements conducted by the NIXE-CAS instrument (see Sec. 3.3) extend the size distribution for large aerosol particles by one size bin with diameters up to 3000 nm. This

325   way, as composite, the largest possible aerosol particle diameter range is covered with measurements which can be achieved from all of the Geophysica instruments. One example of this combined 100 s averaged aerosol size distributions is shown in Fig. 6.

The aerosol particle scattering ratio (SR) is calculated using Eq. 1 with the aerosol backscatter coefficient β_{ap} and the molecular backscatter coefficient β_{mol}.

330    $$SR = \frac{\beta_{ap} + \beta_{mol}}{\beta_{mol}} \tag{1}$$

For every 100 s averaged aerosol size distribution the aerosol backscatter coefficient β_{ap} is calculated based on the Mie-theory as comprehensively described in Cairo et al. (2011). Accounting for the aerosols chemical composition (Höpfner et al. (2019) observed the presence of ammonium nitrate particles), these calculations use a refractive index of 1.5 for the size distributions measured within the ATAL altitude region up to 420 K potential temperature. At Θ levels higher than 420 K a refractive index

335   of 1.45 is used, which better reflects the stratospheric aerosol properties.

To be able to compute the particle scattering ratio, the molecular scattering coefficient β_{mol} for each averaging interval is calculated. Based on Collis and Russell (1976), the simplified method from Cairo et al. (2011) is used together with the temperature and pressure measured by the UCSE system aboard the M55 Geophysica. To be able to compare the resulting SR values with the SR measured by CALIOP, MAS, and MAL, β_{ap} and β_{mol} are calculated using a wavelength of 532 nm.

6.2 Comparison between scattering ratios obtained from in situ and remote sensing data

For a direct comparison between these in situ aerosol size distribution based SR and the aerosol particle SR measured by the satellite-borne lidar CALIOP, a CALIOP data set is needed that was measured within a comparable time period and about the same geographical region as the StratoClim 2017 flight missions. Over the time period from 4 to 31 August 2017 a vertical profile of the aerosol particle SR at a wavelength of 532 nm measured by CALIOP was averaged between 15 to 45 degree North and 70 to 100 degree East. This temporal and horizontal averaging is needed to increase the signal to noise ratio. To be able to detect the ATAL, the CALIOP data set was reanalyzed based on the CALIOP data level 1 V4.10 data set and calibrated between an altitude of 36 to 39 km as previously described by Vernier et al. (2009). During this data processing, backscattering due to ice cloud particles was removed by applying a filter for the volume depolarization ratio within a pixel greater than 5% (Vernier et al. (2011); Vernier et al. (2015)). The vertical profile was then averaged with a vertical resolution of 200 m. Additionally, vertical profiles of the aerosol particle SR at a wavelength of 532 nm measured by the MAS and MAL instruments aboard the M55 Geophysica were averaged over all StratoClim 2017 flight missions. Like for the CALIOP data set a cloud-filter was applied to the MAS and MAL data sets. This filter excludes datapoints with a depolarization ratio greater than 5% and SR values greater than 1.3 for the MAS and greater than 1.4 for the MAL.

Figure 7 shows the averaged CALIOP SR profile represented by the red line in an altitude range from 11 to 21 km. The SR calculated based on the in situ measured aerosol size distributions for the 100 seconds time segments (described in Sec. 6.1) is shown as blue dots. The blue line is the averaged profile for size distribution based calculated SR with a vertical averaging interval of 500 m and with the standard deviation represented by blue horizontal bars. The mean SR profiles measured by the MAS and the MAL are given as green and orange lines, respectively.

At altitudes lower than 13.5 km, the size distribution based SR profile shows smaller values than the CALIOP, MAS and MAL profiles. This can be explained by the frequent appearance of clouds in combination with the fast descent and ascent rates of the M55 Geophysica in this altitude range. Considering the selection criteria for the 100 second time segments described in Sec. 6.1, this leads to only a few valid datapoints in this altitude range. Additionally, the flight segments that are not directly associated with clouds could have been affected previously by scavenging of aerosol particles due to in-cloud processes (Croft et al. (2010); Yang et al. (2015)) that have occurred prior to the observations. The local maximum in the SR profile measured by the MAL in this altitude range might also be considered as an artifact from cloud particles that could not be removed from the signal.

Between 13.5 and about 19 km altitude the SR for the 100 second flight segments scatters around the CALIOP, MAS, and MAL mean profiles with values between 1.01 to over 1.15. Above 14 km altitude its mean SR (blue line) increases from 1.05 parallel with the CALIOP profile (red line) to the maximum of the mean SR of over 1.09 between 17 and 17.5 km altitude. Here it matches the CALIOP SR maximum. The aerosol size distribution shown in Fig. 6 was measured in this altitude range at about 17.5 km altitude and a potential temperature level of 385 K. This 100 s averaged size distribution leads to a calculated SR of 1.12. Above this maximum the SR mean profile from the size distribution based calculations and the CALIOP measurements decrease mostly parallel until 19 km altitude. Between 19 and 21 km altitude the SR of both profiles begins to increase again.

Here, the profiles measured by the MAS and the MAL instruments show the same behavior with a trend to higher SR values.
375 This increase in SR is consistent with the lower part of the Junge Layer. Within the overall picture and under consideration of the standard deviation (blue bars), all four independent methods largely agree with each other. This confirms the ATAL as a layer of enhanced aerosol particle SR, while the altitude range of this observed aerosol layer also agrees very well with the ATAL altitudes between about 14 and 18 km, observed by Vernier et al. (2009), Vernier et al. (2011), Vernier et al. (2015), Brunamonti et al. (2018), and Vernier et al. (2018).

380 **6.3 The ATAL's variability during the StratoClim 2017 campaign period**

Bucci et al. (2020) characterized the StratoClim 2017 campaign period as less convectively active than typically expected during that time of the ASM. They also showed that the second half of the campaign period was more influenced by convection compared to the first half. For this reason, we take a closer look at the differences in aerosol particle SR within the ATAL's altitude range during the first and the second half of the campaign period. The scattering of the size distribution based SR
385 values shows the highly variable nature of the ATAL in time and space. This high variability of the ATAL, even on a day by day basis, was also reported by Hanumanthu et al. (2020) from balloon-borne backscatter measurements conducted during the ASM season 2016. In Fig. 8, the profiles of the aerosol SR derived from the in situ measured size distributions over the full campaign period (a), the first four (b), and the last four (c) of the eight StratoClim 2017 flight missions are shown as blue dots and their corresponding mean profiles as blue lines. The mean profile is only displayed as a line if the corresponding altitude
390 interval includes more than one data point (each resulting from a 100 seconds averaged size distribution). The red lines in Fig. 8 (a), (b), and (c) represent the CALIOP aerosol SR profile for the same time period as discussed in the previous section (4 to 31 August 2017).

During the first four mission flights up to 17 km the mean profile of the aerosol size distribution based SR stays at values between about 1.06 and 1.07, except for a peak between 14 and 15 km altitude. The SR values of the single 100 s segments still
395 scatter widely in this altitude range, with SR between about 1.01 and 1.15. This leaves the CALIOP mean profile for the time period from 4 to 31 August 2017 still in the range of the standard deviation (blue bars). Between 17 and 17.5 km, the mean profile for the first half of the campaign period has a maximum with a SR between 1.07 to 1.08 compared to the maximum of CALIOP measured SR of about 1.09 to 1.10.

Due to the more frequent occurrence of convection during the second half of the campaign period, there are less flight
400 segments available at altitudes of up to about 15 km, where no cloud particles were detected. But above that altitude the SR calculated based on the in situ measured aerosol size distributions are significantly higher compared to the first four campaign mission flights. Between 16 and 17 km altitude its mean profile matches the CALIOP profile with SR values in the range of 1.08 to 1.09 and has a pronounced maximum layer between 17 and 17.5 km altitude. Here, the size distribution based SR mean profile has a maximum SR of 1.14 compared to about 1.09 of the CALIOP mean profile (4 to 31 August 2017). In summary, the
405 direct intercomparison between long time averages of the satellite data and small sets of individual research flights generally is a difficult task. For the ATAL in the Asian Monsoon season of 2017, however, the juxtaposition of the respective measurements

shows that the properties derived from the in situ measured particle size distributions can be broadly reconciled with the satellite observations.

6.4 The ATALs relation to CO and the AMA-centered equivalent latitude

The previous section shows that the intensity of the convective influence has an impact on the characteristics of the ATAL, here discussed in terms of the aerosol particle SR. A commonly used tracer for convective influences on the UT/LS region is an enhancement of the CO mixing ratio (Park et al. (2009); Pan et al. (2016)). Here one has to consider the different timescales of the transport and dilution processes of CO within the UT/LS (tens of days) and aerosol related processes like coagulation and cloud scavenging that can have a significant impact within hours. Furthermore, between June 2006 and August 2008 Vernier et al. (2015) observed a seasonal dependence between the enhanced aerosol SR (measured by CALIOP between 14 and 18 km altitude) and an enhancement of the mean CO mixing ratio near the 100 hPa pressure level, as observed by the satellite-borne Microwave Limb Sounder (MLS, V2.21). They found that during the observed time period the aerosol peak in August was lagging the CO peak by about one month.

Figures 9 (a), (b) and (c) show the correlation between the in situ size distribution based aerosols SR (100 s flight segments) and the averaged CO mixing ratio measured by the COLD2 instrument (described in Sec. 3.6) over the full StratoClim 2017 campaign period, and its first and second half, respectively. For both parts of the campaign, values of the aerosol particle SR larger 1.04 are always associated with CO mixing ratios larger 40 ppb. The flight segments with CO mixing ratios lower than 40 ppb have all been observed associated with potential temperature levels larger 420 K (color-coded), close or above the top of the AMA caused confinement at about 420 to 440 K (Brunamonti et al. (2018); von Hobe et al. (2020)). However, especially Fig 9 (c) shows that the highest CO mixing ratios are not necessarily correlated with a high aerosol SR. The highest values for the aerosol SR (larger than 1.12) observed during the first four flights are accompanied with CO mixing ratios between 70 and 90 ppb and for the last four flights in the range of 50 to 70 ppb.

Besides the strong convective vertical transport associated with the ASM, another feature of the ATAL should be considered, namely the confinement of its air masses within the AMA. This confinement can lead to an accumulation of aerosol particles and trace gases within the AMA region. One measure to relate the geographical position of our measurements to the position of the AMA core and its "border" is the AMA-centered equivalent latitude (EQLAT). The center of the AMA is defined by the lowest values of the potential vorticity (PV) on the 380 K potential temperature level. An equivalent latitude for which 90 degree North corresponds to the center of the AMA was projected for a closed PV contour according to Ploeger et al. (2015). It has to be noted that the definition of the EQLAT is only valid for a range about 20 K above and beneath the 380 K isentrope, as outside this range PV contours in the AMA region are frequently not closed. Furthermore, Ploeger et al. (2015) found that the edge of the confinement caused by the AMA can be determined from a local maximum in the gradient of PV along the 380 K isentrope, and is on average located at around 65 degree EQLAT. The EQLAT is calculated based on the ECMWF ERA-Interim reanalysis.

Figures 9 (d), (e), and (f) show the correlation between the EQLAT and the aerosol particle SR (full campaign period, first half and second half, respectively). While there is no direct correlation between the SR and the EQLAT, high values of aerosol

particle SR (larger 1.08) only occur for flight segments with a EQLAT larger 63 degrees, for the first half of the campaign period (Fig. 9 (a)). During the second half of the StratoClim 2017 campaign aerosol particle SR larger 1.08 were only observed during flight segments with an EQLAT larger 66 degree. This matches well with the edge of the AMAs confinement at about 65 degree EQLAT observed by Ploeger et al. (2015). At high Θ levels above about 420 K (blueish colors) the SR values are

445 always lower than 1.04. This shows that during the ASM typical ATAL aerosol SR values could only be observed horizontally and vertically within the confinement of the AMA.

7   Conclusions

During the 2017 StratoClim field mission in the Asian Summer Monsoon (ASM) season, aerosol measurements were performed over Central Asia up to 20 km altitude aboard the research aircraft M55 Geophysica inside and above the Asian Monsoon

450 Anticyclone (AMA) and the Asian Tropopause Aerosol Layer (ATAL). Here and for the first time, submicrometer sized aerosol size distributions were in situ measured down to 65 nm particle diameter by a modified UHSAS-A optical particle counter. These measurements were conducted in conjunction with condensation particle counters (COPAS), and two near-range remote sensing instruments, MAS and MAL.

   The ATALs aerosol particle scattering ratio (SR) observations by CALIOP during the StratoClim 2017 campaign period, like

455 discussed e.g. by Vernier et al. (2009), Vernier et al. (2011), and Vernier et al. (2018) for previous and recent ASM seasons, could be validated by calculating the SR based on the in situ measured aerosol size distributions, as well as the aerosol particle SR directly measured by the MAS and MAL instruments. All of those four independent methods largely agree with each other and can confirm the ATAL as a layer of enhanced aerosol particle SR within an altitude range from 15 to 18.5 km. The maximum of the ATALs aerosol particle SR signal was observed at 17.5 km altitude, consistently by all four methods.

460 Furthermore, the in situ measurements show that the ATAL is highly variable in time and space and is not a closed, persistent layer. While there is a seasonal correlation between the CO mixing ratio and the ATAL (Vernier et al. (2015)), no direct correlation on the smaller scale, between co-located in situ measurements of the CO mixing ratio and the size distribution based aerosol particle SR, could be found. But, values of SR that are typical for the ATAL could only be observed for CO mixing ratios larger than 40 to 50 ppb. This is also consistent with the observations, that during the StratoClim 2017 campaign

465 period enhanced aerosol particle SR values could only be observed within the confinement of the AMA at a EQLAT larger than 63 degree and below its top of confinement (at about 420 K potential temperature). This regional limitation of the ATAL with respect to the dynamics of the AMA is in good agreement with the horizontal (Ploeger et al. (2015)) and vertical (von Hobe et al. (2020)) limitations of the AMA-caused confinement.

   From the experimental perspective the ATAL is a fairly elusive, highly variable layer situated between approximately 370

470 K ($\approx$ 15 km) and 420 K ($\approx$ 18.5 km) potential temperature. Its lower part is close to –if not still inside- the highest region of convective outflows, while its upper part can be found at tropopause levels (between 369 K and 396 K during StratoClim 2017) or slightly above. Thus the aerosol of the upper ATAL part is subject to very slow -probably spiraling- vertical ascent (with rates of about 1 K potential temperature per day). At the same time, the lower part of the ATAL can be affected by

rapid turbulent mixing which provides precursor gases and aerosols originating from the lower troposphere. In this complex
475   dynamical setting microphysical processes like NPF, aging by coagulation and condensational growth, removal by scavenging
act on the aerosol. The vertical profile of the measured aerosol particle size distributions in combination with the vertical
profiles of the particle mixing ratios from the UHSAS-A and COPAS show a pronounced Aitken-mode between the 350
and 370 K potential temperature levels, i.e. beneath the lower edge of the ATAL. With increasing altitude, the aerosol size
distribution's main mode shifts towards the accumulation mode.

480   Our own simple box model simulations (adopting the SOCOL (SOlar Climate Ozone Links (Stenke et al. (2013)) coagulation
subroutines; see details in Weigel et al. (2020a)) showed that the freshly nucleated aerosol particles (as observed from COPAS)
coagulate onto the background aerosol (as observed by the UHSAS-A) within a few hours. In principle this should affect or
"quench" the frequently occurring NPF events, which were detected by COPAS (Weigel et al. (2020a); Weigel et al. (2020b)).
This suggests that the coagulation of freshly nucleated aerosol particles alone cannot cause the lower part of the aerosol
485   size distribution as measured by the UHSAS-A inside the ATALs altitude range. Also the question remains open, where the
particles larger than roughly 500 to 800 nm in the UHSAS-A size distributions come from. Condensational growth could be
a major process, although the nature and amounts of the various possible condensable gases are not yet well known. Also the
upward transport of already existing larger aerosol particles (Yuan et al. (2019)) can contribute to the overall size distributions
as observed by the UHSAS-A. Because of this complex interaction between dynamical and microphysical processes further,
490   much more advanced model simulations are needed to identify and quantify the importance of various involved processes. To
support such model simulations our data are well suited, because the UHSAS-A particle size distributions extend down to 65
nm while COPAS measured simultaneously with three different lower detection limits from 6 nm up to 15 nm.

Data availability.   The data shown in this study are available at the StratoClim campaign database at
https://stratoclim.icg.kfa-juelich.de/AfcMain/CampaignDataBase or they may be provided by respective PI upon request.

495   *Author contributions.*   CM performed the UHSAS-A measurements and data evaluations, created the figures and draughted the manuscript
with contributions by SB, RW, FC, and JPV. RW provided the COPAS aerosol measurements. FC provided the MAS scattering ratio profile
and performed the scattering ratio calculations based on the prepared aerosol size distributions by CM. JPV provided the CALIOP scattering
ratio profile. VM and RM provided the MAL scattering ratio profile. The NIXE-CAS data was provided by AA and MK. FP contributed with
meteorological re-analyses. SV and FD'A provided the CO data. TD provided the balloon-borne aerosol size distribution measurement data.
500   The manuscript was critically reviewed by RW, FC, JPV, AA, MK, VM, RM, SV, FD'A, FP, TD, and SB.

Competing interests.   The authors declare that they have no conflict of interest.

Acknowledgements. The contributions from the technical staff at the workshops of the MPI for Chemistry and the Institute for Physics of the Atmosphere (Mainz University), as well as the Myasishchev Design Bureau (MDB) were essential. In particular, we acknowledge support of T. Böttger, C. von Glahn, H. Rott, and W. Schneider. The extraordinary commitment of F. Stroh in realisation of the campaign and the leadership of the entire StratoClim project by M. Rex are gratefully acknowledged. We very much thank the MDB crew and the M55 Geophysica pilots. Some of our research leading to the presented results received funding from the European Research Council under the European Union's Seventh Framework Program (FP/2007-2013)/ERC Grant Agreement No. 321040 (EXCATRO). The StratoClim project was funded by the EU (FP7/2007–2018 Grant No. 603557) and also supported by the German "Bundesministerium für Bildung und Forschung" (BMBF) under the joint ROMIC-project SPITFIRE (01LG1205A). The balloon-borne LPC & CNC measurements from Hyderabad were supported by the US National Aeronautics and Space Administration, and from Laramie by the US National Science Foundation, award #1011827. We explicitly thank the Nepalese government authorities, research institutions, and Tribhuvan Airport, as well as the German Embassy for their extraordinary support and hospitality, since without them this exceptional field campaign and our research would not have been possible.

505

510

References

Baumgardner, D., Abel, S. J., Axisa, D., Cotton, R., Crosier, J., Field, P., Gurganus, C., Heymsfield, A., Korolev, A., Krämer, M., Lawson, P., McFarquhar, G., Ulanowski, Z., and Um, J.: Cloud Ice Properties: In Situ Measurement Challenges, Meteorological Monographs, 58, 91–923, https://doi.org/10.1175/amsmonographs-d-16-0011.1, 2017.

Borrmann, S., Kunkel, D., Weigel, R., Minikin, A., Deshler, T., Wilson, J. C., Curtius, J., Volk, C. M., Homan, C. D., Ulanovsky, A., Ravegnani, F., Viciani, S., Shur, G. N., Belyaev, G. V., Law, K. S., and Cairo, F.: Aerosols in the tropical and subtropical UT/LS: in-situ measurements of submicron particle abundance and volatility, Atmospheric Chemistry and Physics, 10, 5573–5592, https://doi.org/10.5194/acp-10-5573-2010, 2010.

Brock, C. A., Hamill, P., Wilson, J. C., Jonsson, H. H., and Chan, K. R.: Particle Formation in the Upper Tropical Troposphere: A Source of Nuclei for the Stratospheric Aerosol, Science, 270, 1650–1653, https://doi.org/10.1126/science.270.5242.1650, 1995.

Brunamonti, S., Jorge, T., Oelsner, P., Hanumanthu, S., Singh, B. B., Kumar, K. R., Sonbawne, S., Meier, S., Singh, D., Wienhold, F. G., Luo, B. P., Boettcher, M., Poltera, Y., Jauhiainen, H., Kayastha, R., Karmacharya, J., Dirksen, R., Naja, M., Rex, M., Fadnavis, S., and Peter, T.: Balloon-borne measurements of temperature, water vapor, ozone and aerosol backscatter on the southern slopes of the Himalayas during StratoClim 2016–2017, Atmospheric Chemistry and Physics, 18, 15 937–15 957, https://doi.org/10.5194/acp-18-15937-2018, 2018.

Bucci, S., Legras, B., Sellitto, P., D'Amato, F., Viciani, S., Montori, A., Chiarugi, A., Ravegnani, F., Ulanovsky, A., Cairo, F., and Stroh, F.: Deep-convective influence on the upper troposphere–lower stratosphere composition in the Asian monsoon anticyclone region: 2017 StratoClim campaign results, Atmospheric Chemistry and Physics, 20, 12 193–12 210, https://doi.org/10.5194/acp-20-12193-2020, 2020.

Cai, Y., Montague, D. C., Mooiweer-Bryan, W., and Deshler, T.: Performance characteristics of the ultra high sensitivity aerosol spectrometer for particles between 55 and 800 nm: Laboratory and field studies, Journal of Aerosol Science, 39, 759 – 769, https://doi.org/10.1016/j.jaerosci.2008.04.007, 2008.

Cairo, F.: Polar stratospheric clouds observed during the Airborne Polar Experiment–Geophysica Aircraft in Antarctica (APE-GAIA) campaign, Journal of Geophysical Research, 109, https://doi.org/10.1029/2003jd003930, 2004.

Cairo, F., Di Donfrancesco, G., Snels, M., Fierli, F., Viterbini, M., Borrmann, S., and Frey, W.: A comparison of light backscattering and particle size distribution measurements in tropical cirrus clouds, Atmospheric Measurement Techniques, 4, 557–570, https://doi.org/10.5194/amt-4-557-2011, 2011.

Campbell, P. and Deshler, T.: Condensation nuclei measurements in the midlatitude (1982-2012) and Antarctic (1986-2010) stratosphere between 20 and 35 km, Journal of Geophysical Research: Atmospheres, 119, 137–152, https://doi.org/10.1002/2013jd019710, 2014.

Collis, R. T. H. and Russell, P. B.: Lidar Measurement of Particles and Gases by Elastic backscattering and Differential absorption, in: Laser Monitoring of the Atmosphere, edited by: Hinkley, E.D., Springer Verlag, Berlin, Germany, https://doi.org/10.1007/3-540-07743-x, 1976.

Costa, A., Meyer, J., Afchine, A., Luebke, A., Günther, G., Dorsey, J. R., Gallagher, M. W., Ehrlich, A., Wendisch, M., Baumgardner, D., Wex, H., and Krämer, M.: Classification of Arctic, midlatitude and tropical clouds in the mixed-phase temperature regime, Atmospheric Chemistry and Physics, 17, 12 219–12 238, https://doi.org/10.5194/acp-17-12219-2017, 2017.

Croft, B., Lohmann, U., Martin, R. V., Stier, P., Wurzler, S., Feichter, J., Hoose, C., Heikkilä, U., van Donkelaar, A., and Ferrachat, S.: Influences of in-cloud aerosol scavenging parameterizations on aerosol concentrations and wet deposition in ECHAM5-HAM, Atmospheric Chemistry and Physics, 10, 1511–1543, https://doi.org/10.5194/acp-10-1511-2010, 2010.

Curtius, J., Weigel, R., Vössing, H.-J., Wernli, H., Werner, A., Volk, C.-M., Konopka, P., Krebsbach, M., Schiller, C., Roiger, A., Schlager, H., Dreiling, V., and Borrmann, S.: Observations of meteoric material and implications for aerosol nucleation in the winter Arctic lower

550   stratosphere derived from in situ particle measurements, Atmospheric Chemistry and Physics, 5, 3053–3069, https://doi.org/10.5194/acp-5-3053-2005, 2005.

Deshler, T., Hervig, M. E., Hofmann, D. J., Rosen, J. M., and Liley, J. B.: Thirty years of in situ stratospheric aerosol size distribution measurements from Laramie, Wyoming (41°N), using balloon-borne instruments, Journal of Geophysical Research: Atmospheres, 108, https://doi.org/10.1029/2002JD002514, 2003.

555   Deshler, T., Luo, B., Kovilakam, M., Peter, T., and Kalnajs, L. E.: Retrieval of Aerosol Size Distributions From In Situ Particle Counter Measurements: Instrument Counting Efficiency and Comparisons With Satellite Measurements, Journal of Geophysical Research: Atmospheres, 124, 5058–5087, https://doi.org/10.1029/2018jd029558, 2019.

Dunkerton, T. J.: Evidence of meridional motion in the summer lower stratosphere adjacent to monsoon regions, Journal of Geophysical Research: Atmospheres, 100, 16 675–16 688, https://doi.org/10.1029/95JD01263, 1995.

560   Fairlie, T. D., Liu, H., Vernier, J.-P., Campuzano-Jost, P., Jimenez, J. L., Jo, D. S., Zhang, B., Natarajan, M., Avery, M. A., and Huey, G.: Estimates of Regional Source Contributions to the Asian Tropopause Aerosol Layer Using a Chemical Transport Model, Journal of Geophysical Research: Atmospheres, 125, https://doi.org/10.1029/2019jd031506, 2020.

Fierli, F., Orlandi, E., Law, K. S., Cagnazzo, C., Cairo, F., Schiller, C., Borrmann, S., Donfrancesco, G. D., Ravegnani, F., and Volk, C. M.: Impact of deep convection in the tropical tropopause layer in West Africa: in-situ observations and mesoscale modelling, Atmospheric

565   Chemistry and Physics, 11, 201–214, https://doi.org/10.5194/acp-11-201-2011, 2011.

Fueglistaler, S., Dessler, A. E., Dunkerton, T. J., Folkins, I., Fu, Q., and Mote, P. W.: Tropical tropopause layer, Reviews of Geophysics, 47, https://doi.org/10.1029/2008RG000267, 2009.

Garny, H. and Randel, W. J.: Transport pathways from the Asian monsoon anticyclone to the stratosphere, Atmospheric Chemistry and Physics, 16, 2703–2718, https://doi.org/10.5194/acp-16-2703-2016, 2016.

570   Hanumanthu, S., Vogel, B., Müller, R., Brunamonti, S., Fadnavis, S., Li, D., Ölsner, P., Naja, M., Singh, B. B., Kumar, K. R., Sonbawne, S., Jauhiainen, H., Vömel, H., Luo, B., Jorge, T., Wienhold, F. G., Dirkson, R., and Peter, T.: Strong variability of the Asian Tropopause Aerosol Layer (ATAL) in August 2016 at the Himalayan foothills, Atmospheric Chemistry and Physics Discussion, https://doi.org/10.5194/acp-2020-552, 2020.

Höpfner, M., Ungermann, J., Borrmann, S., Wagner, R., Spang, R., Riese, M., Stiller, G., Appel, O., Batenburg, A. M., Bucci, S., Cairo,

575   F., Dragoneas, A., Friedl-Vallon, F., Hünig, A., Johansson, S., Krasauskas, L., Legras, B., Leisner, T., Mahnke, C., Möhler, O., Molleker, S., Müller, R., Neubert, T., Orphal, J., Preusse, P., Rex, M., Saathoff, H., Stroh, F., Weigel, R., and Wohltmann, I.: Ammonium nitrate particles formed in upper troposphere from ground ammonia sources during Asian monsoons, Nature Geoscience, 12, 608–612, https://doi.org/10.1038/s41561-019-0385-8, 2019.

Kremser, S., Thomason, L. W., von Hobe, M., Hermann, M., Deshler, T., Timmreck, C., Toohey, M., Stenke, A., Schwarz, J. P., Weigel, R.,

580   Fueglistaler, S., Prata, F. J., Vernier, J.-P., Schlager, H., Barnes, J. E., Antuña-Marrero, J.-C., Fairlie, D., Palm, M., Mahieu, E., Notholt, J., Rex, M., Bingen, C., Vanhellemont, F., Bourassa, A., Plane, J. M. C., Klocke, D., Carn, S. A., Clarisse, L., Trickl, T., Neely, R., James, A. D., Rieger, L., Wilson, J. C., and Meland, B.: Stratospheric aerosol—Observations, processes, and impact on climate, Reviews of Geophysics, 54, 278–335, https://doi.org/10.1002/2015RG000511, 2016.

Mitev, V., Poole, L. R., Pitts, M. C., and Matthey, R.: Comparison Case between CALIPSO Lidar and MALs on M55 Geophysica during

585   RECONCILE Campaign, in: 26th International Laser Radar Conference, 25-29 June 2012, Porto Heli Greece, Proceedings Vol. II, 729-732, 2012.

Mitev, V., Matthey, R., and Makarov, V.: Backscatter-depolarisation lidars on high-altitude research aircraft, in: 20th International Symposium on Atmospheric and Ocean Optics: Atmospheric Physics, edited by Romanovskii, O. A., SPIE, https://doi.org/10.1117/12.2075634, 2014.

Molleker, S., Borrmann, S., Schlager, H., Luo, B., Frey, W., Klingebiel, M., Weigel, R., Ebert, M., Mitev, V., Matthey, R., Woiwode, W., Oelhaf, H., Dörnbrack, A., Stratmann, G., Grooß, J.-U., Günther, G., Vogel, B., Müller, R., Krämer, M., Meyer, J., and Cairo, F.: Microphysical properties of synoptic-scale polar stratospheric clouds: in situ measurements of unexpectedly large HNO$_3$-containing particles in the Arctic vortex, Atmospheric Chemistry and Physics, 14, 10 785–10 801, https://doi.org/10.5194/acp-14-10785-2014, https://acp.copernicus.org/articles/14/10785/2014/, 2014.

Neely, R. R., Yu, P., Rosenlof, K. H., Toon, O. B., Daniel, J. S., Solomon, S., and Miller, H. L.: The contribution of anthropogenic SO2 emissions to the Asian tropopause aerosol layer, Journal of Geophysical Research: Atmospheres, 119, 1571–1579, https://doi.org/10.1002/2013JD020578, 2014.

Pan, L. L., Honomichl, S. B., Kinnison, D. E., Abalos, M., Randel, W. J., Bergman, J. W., and Bian, J.: Transport of chemical tracers from the boundary layer to stratosphere associated with the dynamics of the Asian summer monsoon, Journal of Geophysical Research: Atmospheres, 121, 14,159–14,174, https://doi.org/10.1002/2016jd025616, 2016.

Park, M., Randel, W. J., Gettelman, A., Massie, S. T., and Jiang, J. H.: Transport above the Asian summer monsoon anticyclone inferred from Aura Microwave Limb Sounder tracers, Journal of Geophysical Research: Atmospheres, 112, https://doi.org/10.1029/2006JD008294, 2007.

Park, M., Randel, W. J., Emmons, L. K., and Livesey, N. J.: Transport pathways of carbon monoxide in the Asian summer monsoon diagnosed from Model of Ozone and Related Tracers (MOZART), Journal of Geophysical Research, 114, https://doi.org/10.1029/2008jd010621, 2009.

Ploeger, F., Gottschling, C., Griessbach, S., Grooß, J.-U., Guenther, G., Konopka, P., Müller, R., Riese, M., Stroh, F., Tao, M., Ungermann, J., Vogel, B., and von Hobe, M.: A potential vorticity-based determination of the transport barrier in the Asian summer monsoon anticyclone, Atmospheric Chemistry and Physics, 15, 13 145–13 159, https://doi.org/10.5194/acp-15-13145-2015, 2015.

Prata, A. J., Carn, S. A., Stohl, A., and Kerkmann, J.: Long range transport and fate of a stratospheric volcanic cloud from Soufrière Hills volcano, Montserrat, Atmospheric Chemistry and Physics, 7, 5093–5103, https://doi.org/10.5194/acp-7-5093-2007, 2007.

Randel, W. J. and Jensen, E. J.: Physical processes in the tropical tropopause layer and their roles in a changing climate, Nature Geoscience, 6, 169, https://doi.org/10.1038/ngeo1733, 2013.

Randel, W. J. and Park, M.: Deep convective influence on the Asian summer monsoon anticyclone and associated tracer variability observed with Atmospheric Infrared Sounder (AIRS), Journal of Geophysical Research, 111, https://doi.org/10.1029/2005jd006490, 2006.

Sokolov, L. and Lepuchov, B.: Protocol of interaction between Unit for Connection with Scientific Equipment (UCSE) and on-board scientific equipment of Geophysica aircraft (Second edition), 1998.

Stenke, A., Schraner, M., Rozanov, E., Egorova, T., Luo, B., and Peter, T.: The SOCOL version 3.0 chemistry–climate model: description, evaluation, and implications from an advanced transport algorithm, Geoscientific Model Development, 6, 1407–1427, https://doi.org/10.5194/gmd-6-1407-2013, 2013.

Vernier, J. P., Pommereau, J. P., Garnier, A., Pelon, J., Larsen, N., Nielsen, J., Christensen, T., Cairo, F., Thomason, L. W., Leblanc, T., and McDermid, I. S.: Tropical stratospheric aerosol layer from CALIPSO lidar observations, Journal of Geophysical Research, 114, https://doi.org/10.1029/2009jd011946, 2009.

Vernier, J.-P., Thomason, L. W., and Kar, J.: CALIPSO detection of an Asian tropopause aerosol layer, Geophysical Research Letters, 38, https://doi.org/10.1029/2010GL046614, 2011.

625 Vernier, J.-P., Fairlie, T. D., Natarajan, M., Wienhold, F. G., Bian, J., Martinsson, B. G., Crumeyrolle, S., Thomason, L. W., and Bedka, K. M.: Increase in upper tropospheric and lower stratospheric aerosol levels and its potential connection with Asian pollution, Journal of Geophysical Research: Atmospheres, 120, 1608–1619, https://doi.org/10.1002/2014jd022372, 2015.

Vernier, J.-P., Fairlie, T. D., Deshler, T., Ratnam, M. V., Gadhavi, H., Kumar, B. S., Natarajan, M., Pandit, A. K., Raj, S. T. A., Kumar, A. H., Jayaraman, A., Singh, A. K., Rastogi, N., Sinha, P. R., Kumar, S., Tiwari, S., Wegner, T., Baker, N., Vignelles, D., Stenchikov, G.,
630 Shevchenko, I., Smith, J., Bedka, K., Kesarkar, A., Singh, V., Bhate, J., Ravikiran, V., Rao, M. D., Ravindrababu, S., Patel, A., Vernier, H., Wienhold, F. G., Liu, H., Knepp, T. N., Thomason, L., Crawford, J., Ziemba, L., Moore, J., Crumeyrolle, S., Williamson, M., Berthet, G., Jégou, F., and Renard, J.-B.: BATAL: The Balloon Measurement Campaigns of the Asian Tropopause Aerosol Layer, Bulletin of the American Meteorological Society, 99, 955–973, https://doi.org/10.1175/bams-d-17-0014.1, 2018.

Viciani, S., D'Amato, F., Mazzinghi, P., Castagnoli, F., Toci, G., and Werle, P.: A cryogenically operated laser diode spectrometer for airborne
635 measurement of stratospheric trace gases, Applied Physics B, 90, 581–592, https://doi.org/10.1007/s00340-007-2885-2, 2008.

Viciani, S., Montori, A., Chiarugi, A., and D'Amato, F.: A Portable Quantum Cascade Laser Spectrometer for Atmospheric Measurements of Carbon Monoxide, Sensors, 18, 2380, https://doi.org/10.3390/s18072380, 2018.

Vogel, B., Günther, G., Müller, R., Grooß, J.-U., and Riese, M.: Impact of different Asian source regions on the composition of the Asian monsoon anticyclone and of the extratropical lowermost stratosphere, Atmospheric Chemistry and Physics, 15, 13 699–13 716,
640 https://doi.org/10.5194/acp-15-13699-2015, 2015.

Vogel, B., Müller, R., Günther, G., Spang, R., Hanumanthu, S., Li, D., Riese, M., and Stiller, G. P.: Lagrangian simulations of the transport of young air masses to the top of the Asian monsoon anticyclone and into the tropical pipe, Atmospheric Chemistry and Physics, 19, 6007–6034, https://doi.org/10.5194/acp-19-6007-2019, 2019.

von Hobe, M., Ploeger, F., Konopka, P., Kloss, C., Ulanowski, A., Yushkov, V., Ravegnani, F., Volk, C. M., Pan, L. L., Honomichl, S. B.,
645 Tilmes, S., Kinnison, D. E., Garcia, R. R., and Wright, J. S.: Upward transport into and within the Asian monsoon anticyclone as inferred from StratoClim trace gas observations, Atmospheric Chemistry and Physics Discussion, https://doi.org/10.5194/acp-2020-891, 2020.

Wagner, R., Bertozzi, B., Höpfner, M., Höhler, K., Möhler, O., Saathoff, H., and Leisner, T.: Solid Ammonium Nitrate Aerosols as Efficient Ice Nucleating Particles at Cirrus Temperatures, Journal of Geophysical Research: Atmospheres, 125, https://doi.org/10.1029/2019jd032248, 2020.

650 Ward, S. M., Deshler, T., and Hertzog, A.: Quasi-Lagrangian measurements of nitric acid trihydrate formation over Antarctica, Journal of Geophysical Research: Atmospheres, 119, 245–258, https://doi.org/10.1002/2013JD020326, 2014.

Weigel, R., Hermann, M., Curtius, J., Voigt, C., Walter, S., Böttger, T., Lepukhov, B., Belyaev, G., and Borrmann, S.: Experimental characterization of the COndensation PArticle counting System for high altitude aircraft-borne application, Atmospheric Measurement Techniques, 2, 243–258, https://doi.org/10.5194/amt-2-243-2009, 2009.

655 Weigel, R., Borrmann, S., Kazil, J., Minikin, A., Stohl, A., Wilson, J. C., Reeves, J. M., Kunkel, D., de Reus, M., Frey, W., Lovejoy, E. R., Volk, C. M., Viciani, S., D'Amato, F., Schiller, C., Peter, T., Schlager, H., Cairo, F., Law, K. S., Shur, G. N., Belyaev, G. V., and Curtius, J.: In situ observations of new particle formation in the tropical upper troposphere: the role of clouds and the nucleation mechanism, Atmospheric Chemistry and Physics, 11, 9983–10 010, https://doi.org/10.5194/acp-11-9983-2011, 2011.

Weigel, R., Volk, C. M., Kandler, K., Hösen, E., Günther, G., Vogel, B., Grooß, J.-U., Khaykin, S., Belyaev, G. V., and Borrmann, S.:
660 Enhancements of the refractory submicron aerosol fraction in the Arctic polar vortex: feature or exception?, Atmospheric Chemistry and Physics, 14, 12 319–12 342, https://doi.org/10.5194/acp-14-12319-2014, 2014.

Weigel, R., Mahnke, C., Baumgartner, M., Dragoneas, A., Vogel, B., Ploeger, F., Viciani, S., D'Amato, F., Bucci, S., Legras, B., Luo, B., and Borrmann, S.: In-Situ observation of New Particle Formation in the upper troposphere / lower stratosphere of the Asian Monsoon Anticyclone, Atmospheric Chemistry and Physics Discussion, in review, https://doi.org/10.5194/acp-2020-1158, 2020a.

665   Weigel, R., Mahnke, C., Baumgartner, M., Krämer, M., Spichtinger, P., Spelten, N., Afchine, A., Rolf, C., Viciani, S., D'Amato, F., Tost, H., and Borrmann, S.: New particle formation inside ice clouds: in situ observations in the tropical tropopause layer of the 2017 Asian Monsoon Anticyclone, Atmospheric Chemistry and Physics Discussion, acp-2020-1285, 2020b.

Williamson, C. J., Kupc, A., Axisa, D., Bilsback, K. R., Bui, T., Campuzano-Jost, P., Dollner, M., Froyd, K. D., Hodshire, A. L., Jimenez, J. L., Kodros, J. K., Luo, G., Murphy, D. M., Nault, B. A., Ray, E. A., Weinzierl, B., Wilson, J. C., Yu, F., Yu, P., Pierce, J. R.,

670   and Brock, C. A.: A large source of cloud condensation nuclei from new particle formation in the tropics, Nature, 574, 399–403, https://doi.org/10.1038/s41586-019-1638-9, 2019.

Winker, D. M., Pelon, J., Coakley, J. A., Ackerman, S. A., Charlson, R. J., Colarco, P. R., Flamant, P., Fu, Q., Hoff, R. M., Kittaka, C., Kubar, T. L., Treut, H. L., Mccormick, M. P., Mégie, G., Poole, L., Powell, K., Trepte, C., Vaughan, M. A., and Wielicki, B. A.: The CALIPSO Mission, Bulletin of the American Meteorological Society, 91, 1211–1230, https://doi.org/10.1175/2010bams3009.1, 2010.

675   Yang, Q., Easter, R. C., Campuzano-Jost, P., Jimenez, J. L., Fast, J. D., Ghan, S. J., Wang, H., Berg, L. K., Barth, M. C., Liu, Y., Shrivastava, M. B., Singh, B., Morrison, H., Fan, J., Ziegler, C. L., Bela, M., Apel, E., Diskin, G. S., Mikoviny, T., and Wisthaler, A.: Aerosol transport and wet scavenging in deep convective clouds: A case study and model evaluation using a multiple passive tracer analysis approach, Journal of Geophysical Research: Atmospheres, 120, 8448–8468, https://doi.org/10.1002/2015jd023647, 2015.

Yu, P., Toon, O. B., Neely, R. R., Martinsson, B. G., and Brenninkmeijer, C. A. M.: Composition and physical properties of the

680   Asian Tropopause Aerosol Layer and the North American Tropospheric Aerosol Layer, Geophysical Research Letters, 42, 2540–2546, https://doi.org/10.1002/2015gl063181, 2015.

Yu, P., Rosenlof, K. H., Liu, S., Telg, H., Thornberry, T. D., Rollins, A. W., Portmann, R. W., Bai, Z., Ray, E. A., Duan, Y., Pan, L. L., Toon, O. B., Bian, J., and Gao, R.-S.: Efficient transport of tropospheric aerosol into the stratosphere via the Asian summer monsoon anticyclone, Proceedings of the National Academy of Sciences, 114, 6972–6977, https://doi.org/10.1073/pnas.1701170114, 2017.

685   Yuan, C., Lau, W. K. M., Li, Z., and Cribb, M.: Relationship between Asian monsoon strength and transport of surface aerosols to the Asian Tropopause Aerosol Layer (ATAL): interannual variability and decadal changes, Atmospheric Chemistry and Physics, 19, 1901–1913, https://doi.org/10.5194/acp-19-1901-2019, 2019.
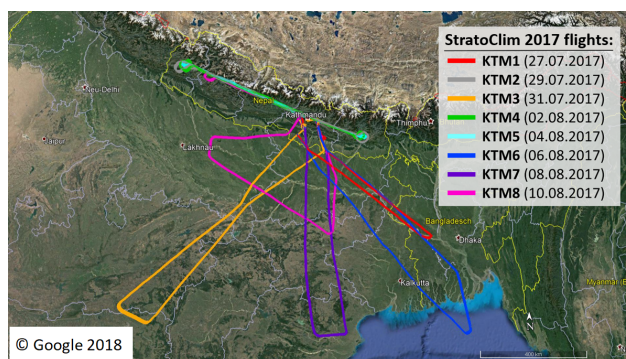
Figure 1. All flight paths of the mission flights conducted in Kathmandu (Nepal) as part of the StratoClim 2017 measurement campaign. GPS data from UCSE, Copyright: © Google 2018.
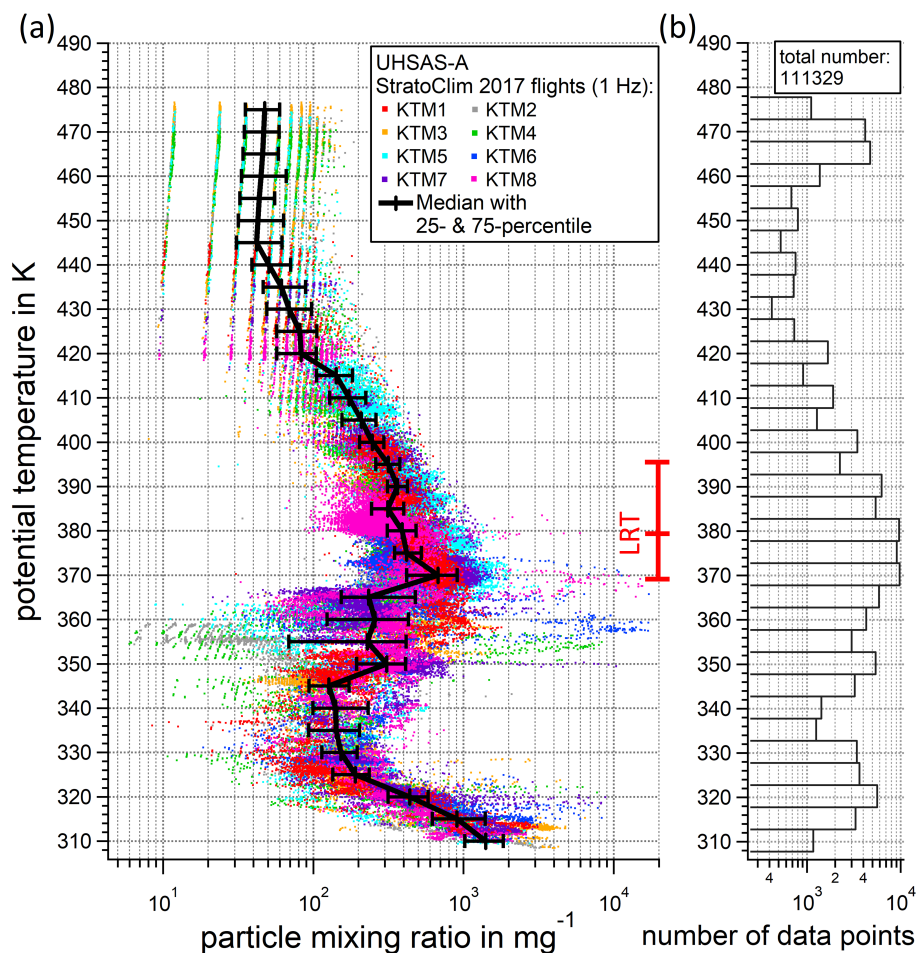
Figure 2. Panel (a): Vertical profile of the particle mixing ratio measured with the UHSAS-A (diameter range: 65 - 1000 nm) during the StratoClim 2017 measurement campaign, with the potential temperature as vertical coordinate. The 1 Hz resolved data points of the individual measurement flights are marked by individually colored dots. In black the median profile of all flights is plotted in steps of 5 K (each over a $\pm$ 2.5 K interval) with the 25 % and 75 % percentiles. The red vertical bar indicates the position (minimum, mean, maximum Θ level) of the lapse rate tropopause (LRT; calculated from the reanalysis data) during the campaign period. Panel (b): The number of 1 Hz data points included in each 5 K potential temperature interval.
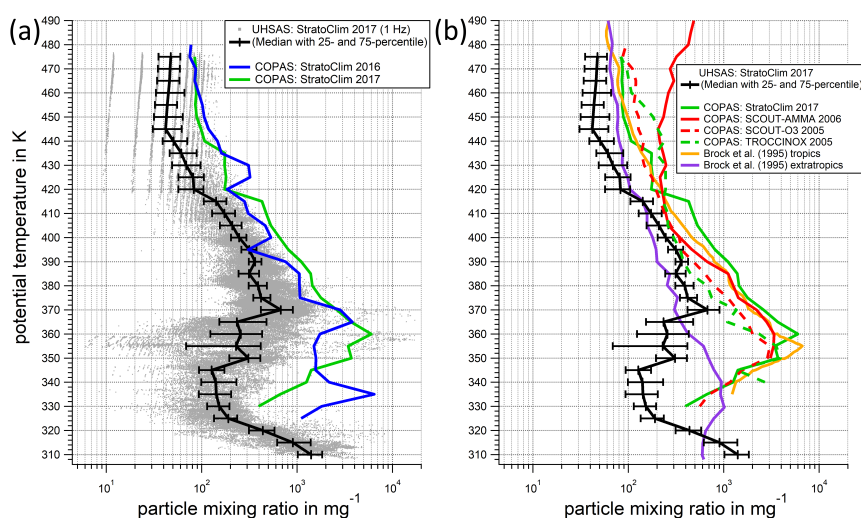
Figure 3. Vertical profile of the particle mixing ratio with the potential temperature as vertical coordinate. Panel (a) shows the 1 Hz resolved particle mixing ratios measured with the UHSAS-A (diameter range: 65 - 1000 nm) during StratoClim 2017 as gray dots. In black, the median profile of all flights is plotted in steps of 5 K (each over a $\pm$ 2.5 K interval) with the 25 % and 75 % percentiles. The median profile of the particle mixing ratio measured by the COPAS (diameter range: 10 - 1000 nm) during the StratoClim 2016 measurement campaign in the extratropics (Kalamata, Greece) is shown in blue, the profile measured during StratoClim 2017 (Kathmandu, Nepal) in the tropics in in green. Panel (b) includes the median profile (with the 25 % and 75 % percentiles) of particle mixing ratio measured with the UHSAS-A during StratoClim 2017 (black line), the median profiles measured by COPAS for particle diameters larger 10 nm during StratoClim 2017 (Nepal, green line), SCOUT-AMMA 2006 (West Africa, red line), SCOUT-O3 2005 (Australia, red dotted line), and for diameter larger 6 nm during TROCCINOX 2005 (Brazil, green dotted line) as depicted in Borrmann et al. (2010). The median profiles, read out of Fig.1 from the publication by Brock et al. (1995), for the tropics are plotted as an orange line and for the extratropics as a purple line.
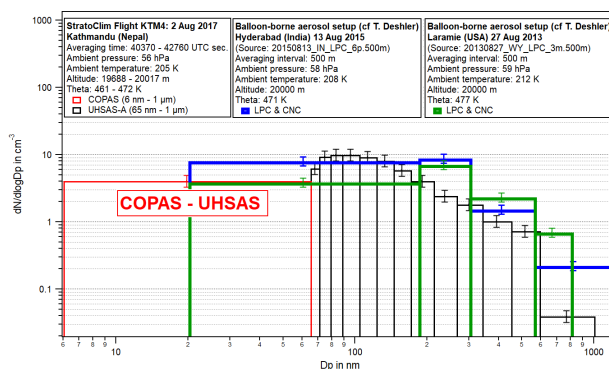
Figure 4. Aerosol particle size distribution combined from the measurements performed by the UHSAS-A and COPAS for the highest flight level reached during the flight KTM4 of the 2017 StratoClim campaign. The particle number concentrations are given for ambient conditions. The concentration of the red marked size bin (6 nm to 65 nm) is the difference of the total number concentrations measured by COPAS (diameter range: 6 nm to 1000 nm) and UHSAS-A (diameter range: 65 nm to 1000 nm). Air pressure, temperature, altitude, and potential temperature according to the UCSE data set. For comparison, measurements of the balloon-borne measurement set-up described by Ward et al. (2014) and Campbell and Deshler (2014) of flights from Hyderabad (India) and from Laramie (USA) are shown in blue and green, respectively.
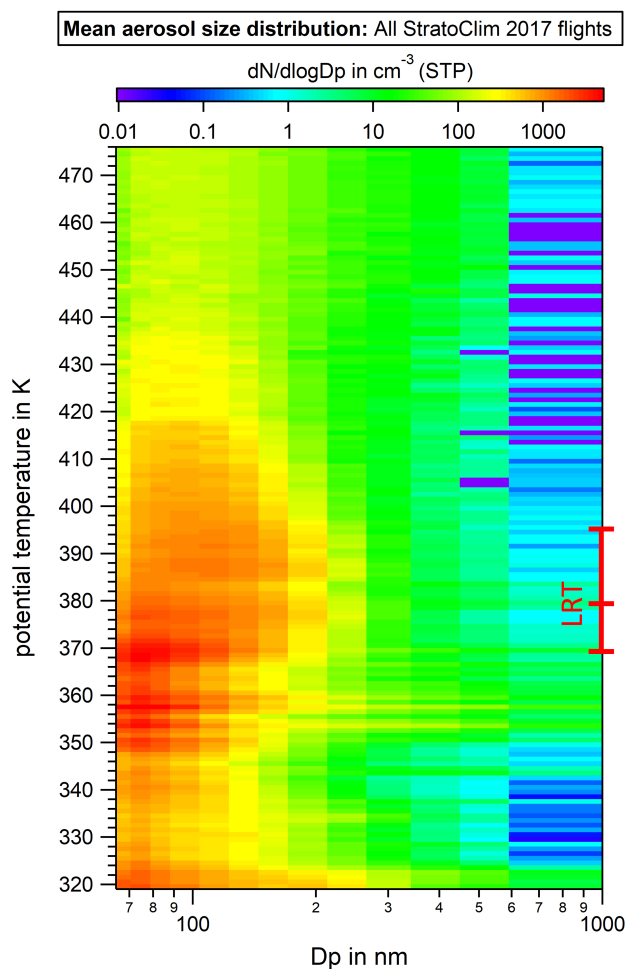
Figure 5. Vertical profile of the aerosol particle size distribution measured by the UHSAS-A during the 2017 StratoClim field campaign averaged over 1 K potential temperature intervals. The color-coded particle number concentrations for each size-bin are converted from ambient conditions to Standard Temperature and Pressure (STP). The red vertical bar indicates the position (minimum, mean, maximum Θ level) of the lapse rate tropopause (LRT; calculated from the reanalysis data) during the campaign period.
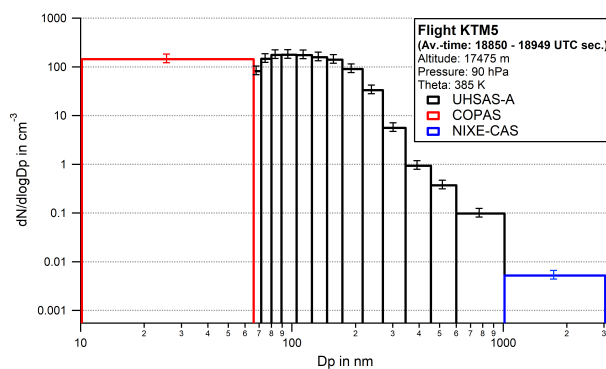
Figure 6. Aerosol particle size distribution measured within the ATAL during flight KTM5 of the 2017 StratoClim measurement campaign. Combined out of the measurements conducted by the COPAS (red size-bin), the UHSAS-A (black size-bins), and the NIXE-CAS (blue size-bin).
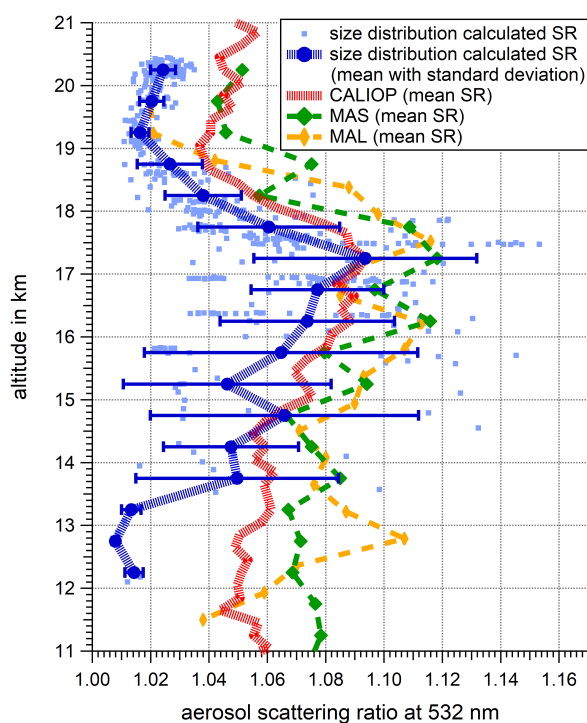
Figure 7. Vertical profile of the aerosol particle scattering ratio at 532 nm wavelength. Calculated based on the aerosol size distributions measured during the 2017 StratoClim measurement campaign as blue dots (100 s averages) and mean profile (blue line) with standard deviation (blue bars). The mean profiles of the scattering ratio at 532 nm wavelength measured by CALIOP, MAS, and MAL are plotted in red, green and orange, respectively.
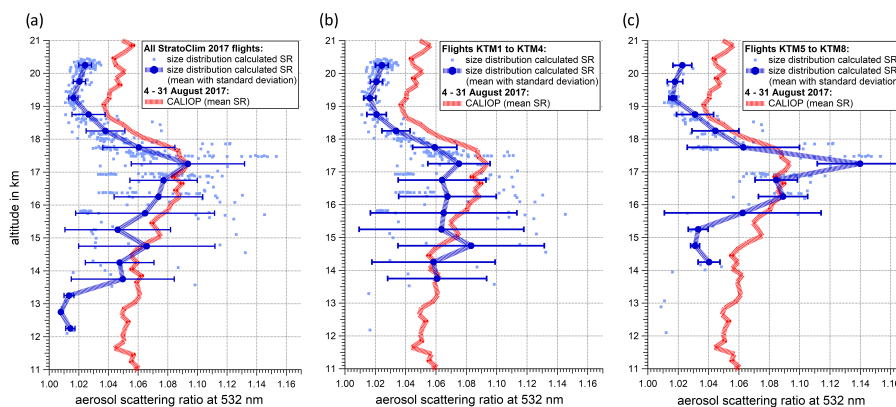
Figure 8. Vertical profile of the aerosol particle scattering ratio at 532 nm wavelength, calculated based on the aerosol size distributions measured during the 2017 StratoClim measurement campaign as blue dots (100 s averages) and mean profile (blue line) with standard deviation (blue bars). Panel (a) represents the full period of the 2017 StratoClim field campaign, panel (b) the first half (flights KTM1 to KTM4), and panel (c) the second half (flights KTM5 to KTM8) of the campaign period. The red lines in panel (a), (b), and (c) represent the vertical mean SR profile measured by CALIOP between 4 and 31 August 2017.
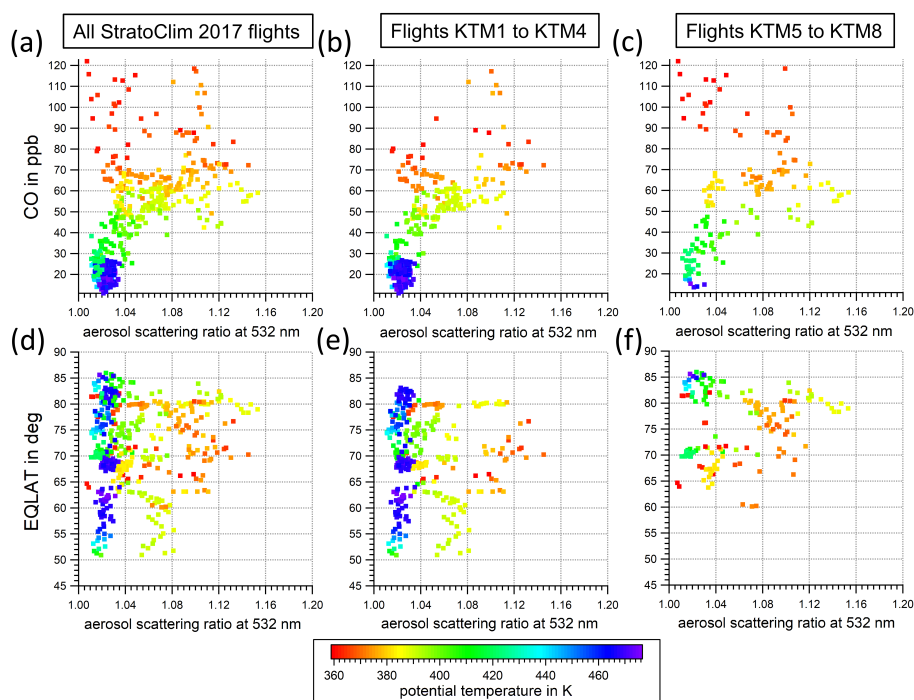
Figure 9. Correlations between the size distribution based aerosol particle SR with the CO mixing ratio (panels (a), (b), and (c)) and the AMA-centered equivalent latitude (EQLAT) (panels (d), (e), and (f)). Panels (a), (d) represents the full period of the 2017 StratoClim field campaign, panels (b), (e) the first half (flights KTM1 to KTM4), and panels (c), (f) the second half (flights KTM5 to KTM8) of the campaign period. The potential temperature is color-coded.